ELSEVIER

Journal of Fluids and Structures 24 (2008) 778–798

JOURNAL OF FLUIDS AND STRUCTURES

www.elsevier.com/locate/jfs

Two noncircular cross-section bodies and a high wing-body configuration at incidence in a low subsonic free stream

D.K. Pantelatos, D.C. Tzotzolakis, D.S. Mathioulakis*

School of Mechanical Engineering/Fluids Section, National Technical University of Athens, 9 Heröon Polytechniou Avenue, 15710 Zografos, Athens, Greece

Available online 24 April 2008

Abstract

This experimental study examines the flow characteristics over a square cross-section body with sharp edges, a rectangular one with rounded edges, and a high wing-body configuration, in a low subsonic free stream. Pressure, velocity, force measurements and flow visualization provide a picture of the flow behaviour, locally and globally. Flow visualization and velocity measurements clearly depict the presence of two axial counter-rotating vortices in the leeside of the first two bodies, being mainly responsible for the asymmetric loading at nonzero roll angles, maximizing the side-force at a roll angle of about 25°. For all body orientations there is always a recirculation region at the nose-afterbody junction leeside area, the extent of which depends mainly on the roll angle. Pressure gradients take high values at the corners of the after body cross-section, even when these are rounded. No asymmetries were practically detected for a zero roll angle and pitch angles up to 20° for the examined three models. The wing-body configuration exhibits a higher lift slope and a more negative zero lift angle, compared to the wing-alone case, and the side-force increases monotonically with the roll angle, without showing any maximum in contrast to the other two models.

Keywords: Non-axisymmetric body; Asymmetric loading; Cross-flow vortices; NACA4415 airfoil; High-wing configuration; UAV

1. Introduction

The use of noncircular cross-section shapes in the design of missiles and unmanned aerial vehicles (UAV) is due to both their stealth characteristics and the optimum utilization of the available internal space for a given frontal area.

With regard to their aerodynamic behaviour, square or rectangular cross-section bodies present higher normal forces compared to axisymmetric ones. However, they are exposed to undesirable side-forces when rolled, in contrast to the axisymmetric bodies, whose aerodynamics is roll independent, unless their nose is quite sharp and the angle of attack high (Lamont, 1982; Ericson and Reding, 1986). Rounding the edges of the noncircular section, both the lift and side-force are reduced, tending to behave like a circular one (Schneider, 1982).

The prominent feature of the flow field around a rectangular cross-section fuselage is the presence of two counter-rotating vortices on its leeward side, the strength of which increases with both the pitch and roll angles (Lijewski et al., 1982; Wilcox et al., 2004). The generation of the side-force is mainly due to asymmetric vortex location which maximizes at a roll angle of 22.5° (Lijewski et al., 1982). At this particular roll angle, one vortex is closer to the body

*Corresponding author.
E-mail address: mathew@fluid.mech.ntua.gr (D.S. Mathioulakis).

0889-9746/$ - see front matter © 2008 Elsevier Ltd. All rights reserved.
doi:10.1016/j.jfluidstructs.2007.12.009

Nomenclature

A	wing aspect ratio
b	wing span
b_f	spanwise length of the wing portion attached to the fuselage
c	wing chord length
C	area of wind tunnel cross-section
C_D	drag coefficient, D/qS
C'_D	corrected drag coefficient due to solid and wake blockage
C^*_D	uncorrected drag coefficient
C^*_{D0}	uncorrected drag coefficient for zero lift
C^*_{Di}	uncorrected vortex drag coefficient
C_L	lift coefficient, L/qS, where S the reference area
C^*_L	uncorrected lift coefficient
C'_L	corrected lift coefficient due to solid and wake blockage
$C_{L\alpha}$	wing lift slope for infinite wing span
$C_{Lw\alpha}$	wing lift slope for finite wing span
C_{Lwf}	lift coefficient of the wing-fuselage configuration
c_p	pressure coefficient, $(p-p_\infty)/q$
C_y	side-force coefficient, Y/qS
D	drag
I_w	angle between wing chord and fuselage longitudinal axis
ℓ_A	length of model "A"
ℓ_B	length of model "B"
ℓ_{rA}	reference length for model "A"
ℓ_{rB}	reference length for model "B"
L	lift
p	static pressure
p_∞	free-stream static pressure
q	free-stream dynamic pressure
Re	Reynolds number
R_l	windward side corner radius
R_u	leeside corner radius
S	reference area
S_B	reference area for model "B"
S_{net}	wing planform area reduced by its part which is attached to the fuselage
S_w	wing planform area
U^*	uncorrected free-stream velocity
V_B	volume of model "B"
V_w	wing volume
x	axial distance from nose tip
Y	side-force
α	corrected pitch angle
α^*	geometric pitch angle
α_0	wing zero-lift angle
ΔU	free-stream velocity increase due to blockage
θ	yaw angle
ν	air kinematic viscosity
φ	roll angle

compared to the other, thus inducing low pressures on one side and high pressures on the opposite side of the body. On the contrary, at a roll angle of 45° both vortices are strong and symmetrically positioned with respect to the diagonal of the cross-section. As a consequence, the side-force is minimized and the normal force is maximized due to the low pressures induced by the vortices. Increasing the roll angle to more than 45°, the locations of the vortex cores change in such a way that the side-force direction reverses (Schneider, 1982). These flow patterns have been observed in both low subsonic (Lijewski et al., 1982; Daniel et al., 1982) and supersonic regimes (Schneider, 1982; Wilcox et al., 2004). When the corners of the cross-section are not sharp, the formed vortices are weak and close to the body surface, thus reducing any asymmetric loading. This was experimentally demonstrated by Lijewski et al. (1982) and Schneider (1982) for square and rectangular cross-sections of various corner radii as well as for circular cross-section bodies. With regard to the Reynolds number effect, Daniel et al. (1984) showed experimentally that the normal force coefficient of a square cross-section body depends on the roll angle; namely, for a zero roll angle this is essentially independent of Re, whereas for a 45° roll angle normal force coefficient exhibits a transition type reduction, as it occurs in circular bodies.

The scope of the present study is the experimental investigation of the flow field about bodies of noncircular cross-section at low speeds. This information is related amongst other to UAVs, the utilization of which has been increased nowadays, because of their advantages compared to conventional air vehicles.

Three models are examined in this work, namely a square cross-section body with sharp edges, named "model A" for brevity, a rectangular cross-section body with rounded edges, "model B", and a combination of the latter body with a wing positioned on top of it, named "model C".

2. Models and methods

This work was initiated due to the need for a change of the fuselage shape of an existing UAV; namely, its initial circular cross-section had to be changed to a rectangular one. Therefore, the aerodynamics of the new configuration had to be examined before integrating the new fuselage into the original vehicle.

In order to gain an insight into the physics of flow about bodies with fuselages of noncircular cross-section, a square cross-section fuselage model (model A) was first examined. It was decided to make its corners sharp, so that the flow field is Reynolds number independent as far as the flow separation lines are concerned, and the generated vortices are easily identified. Following the same notion, its nose was composed of four flat surfaces connected along sharp edges. This model had a 30 mm × 30 mm cross-section and a total length $\ell_A = 180$ mm. In Fig. 1, two views of this model are shown, namely the side view (Fig. 1(a)) and the top view (Fig. 1(b)), as well as the cross-section of the afterbody (Fig. 1(c)). It was made of bronze, mounted on a suitable mechanism, which allowed the adjustment of both the pitch angle ($\alpha = 0$–30° in 10° steps) and roll angle ($\varphi = 0$–60° in 20° steps), independently. A positive pitch angle increment corresponded to an upwards motion of the body nose, whereas a positive roll angle to a starboard rotation about the body longitudinal axis. Due to the small size of the model, only 12 pressure orifices were opened along the perimeter of a cross-section, namely three along each side (one at the middle and two others 5 mm far from each corner). The longitudinal position of this station was 30 mm upstream of the model base, namely at $x = 150$ mm, where x is the distance from the nose tip. Fig. 2 illustrates the locations of the pressure orifices with their numbering and the orientation of the cross section for an arbitrary roll angle, φ. At 0° roll angle, pressure ports 1–3 belong to the leeward side of the model (side A) and 7–9 to the windward one (side C). The surface static pressures were measured by capacitance type linear transducers, the output signals of which were digitized by an A/D converter. Prior to each experiment, a calibration of all transducers took place. The uncertainty of the pressure measurements is estimated to be ± 2 Pa.

The flow field about this model was examined in an open circuit wind tunnel with a cross-section of 420 mm (horizontal) × 230 mm (vertical) at a mean free-stream velocity of 17 m/s with a maximum variation of 0.5% and a turbulence level of 0.3% (measured with a single hot-wire probe). The free-stream velocity was continuously monitored by a Pitot-static tube, located 5 model lengths upstream of the model nose tip.

The velocity field (three velocity components) was measured via a seven-hole Pitot tube (Aeroprobe Corp.) on a plane perpendicular to the free stream (vertical plane) 10 mm downstream of the model base area. It was decided to conduct these measurements downstream of the model, so that the probe does not approach the model walls, thus minimizing its influence on the flow field. Moreover, flow visualization at this plane revealed that the leeside vortices were stable for the examined free-stream conditions. The calibration of the probe was done by Aeroprobe Corp. for a Mach number 0.07 following the procedure described by Johansen et al. (2001). The probe was mounted on a traversing mechanism in such a way that the orientation of the pressure orifices coincided with that one when the calibration took place. Using the calibration database of this probe, flow angularities up to 70° could be measured. Seven flexible tubes, 400 mm long, connected the probe ports to seven linear pressure transducers, the calibration of which was done prior to each experiment. The probe was translated by an automated two-directional traversing mechanism with a minimum step of 3 mm, equal to the probe diameter. The total area covered by the probe was 120 mm horizontally by 60 mm vertically through 760 points.

In order to obtain a qualitative picture of the flow around the body, smoke visualization was used, employing an Argon Ion Laser continuous light source, whereas an oil–TiO_2 mixture film was applied on the model surface for surface visualization. A CCD camera was installed downstream of the model, outside the tunnel, recording the smoke images in a video recorder with a rate of 25 frames per second. In order to obtain a good picture of the cross-flow development over the whole length of the body, the laser sheet, which was perpendicular to the free-stream direction, was moved to several cross-sections along the body longitudinal axis.

"Model B" was made of wood, with a rectangular cross-section of 210 mm (horizontal) × 260 mm (vertical) with rounded edges and a total length $\ell_B = 1300$ mm. The corner radius at the leeside was $R_u = 35$ mm and at the windward side $R_\ell = 25$ mm. Fig. 3 includes the side view of the model (vertical plane of symmetry) and its picture in the wind tunnel horizontal test-section. This body represented the fuselage of an existing UAV at $\frac{1}{2}$-scale. It was mounted on a vertical sting located 200 mm downstream of the model base area. This sting was connected to the six-component strain gauge balance of a closed circuit wind tunnel (NTUA Aerodynamics Laboratory). A rotation of this sting about its axis allowed the adjustment of the model yaw angle. Positive yaw angles corresponded to a motion of the model nose to the right (starboard side). A mechanism allowed the rotation of the model about both its longitudinal axis (roll angle, see Fig. 3) and a horizontal axis (pitch angle). Pitch, roll and yaw angles were varied in the range 0–20°, 0–45° and 0–10°, respectively. Positive pitch angles corresponded to an upwards motion of the model nose, and positive roll angles to a clockwise rotation about the model longitudinal axis. The cross-section of the wind tunnel test-section is rectangular, 1800 mm (horizontal) × 1400 mm (vertical) with chamfered corners. The free-stream velocity measured with a Pitot-static tube was adjusted to be 20 m/s with a maximum variation of 1% and its turbulence level did not exceed 0.2%. The three force components, namely lift (vertical, normal to the free stream), drag (horizontal, along the streamwise direction) and side-force (horizontal, normal to the free stream) were measured with an accuracy of ± 2 N.

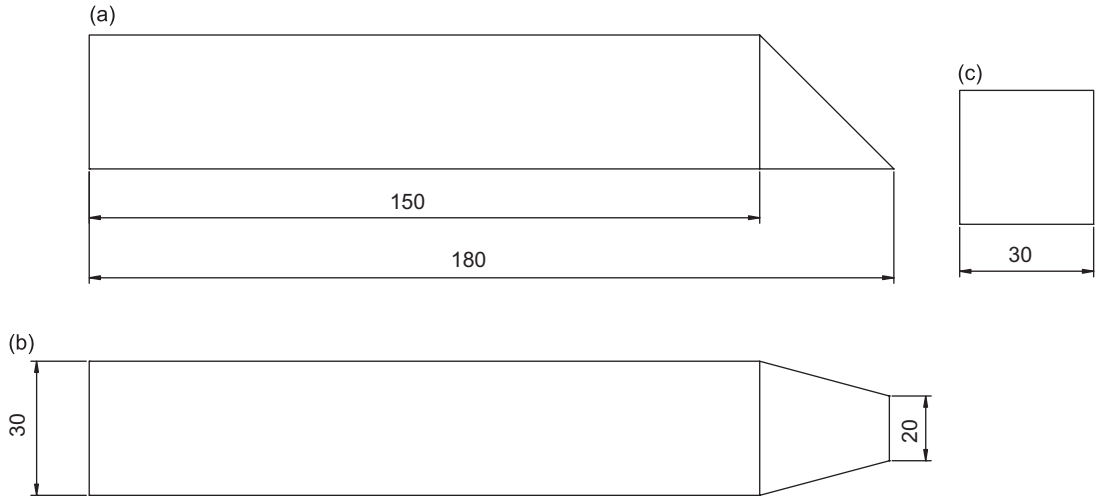

Fig. 1. Model A: (a) side view, (b) top view, and (c) cross-section; dimensions in mm.

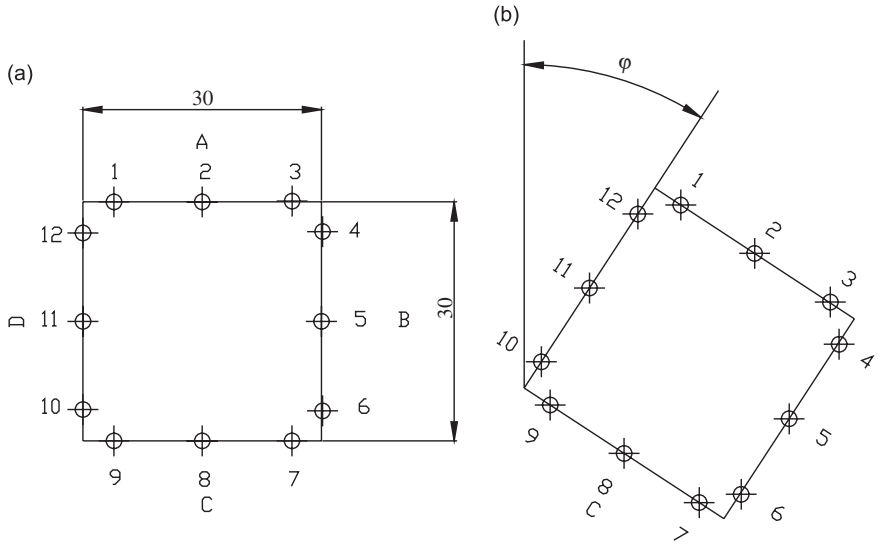

Fig. 2. Model A: locations of pressure orifices: (a) roll angle zero and (b) roll angle φ.

Pressure distribution in the nose area of the model was measured through 41 pressure orifices along four lines (Fig. 4) belonging to two mutually perpendicular planes. One of these planes constitutes the plane of symmetry of the model shown in Fig. 3. Also, the pressure distribution was measured along the perimeter of two cross-sections in the afterbody. The first of these cross-sections was at the junction of the nose with the afterbody ($x = 290$ mm) and the second one at $x = 590$ mm. The two cross-sections are shown in Fig. 5, as well as the exact locations of the pressure orifices. A 48-port scanivalve located inside the model was used to record the pressure signals ($p-p_\infty$) digitized by an A/D converter. The pressure p_∞ was measured by a Pitot-static tube located upstream of the model. The pressure transducer of the scanivalve had an uncertainty of ± 2 Pa.

"Model C" consisted of "Model B" and a NACA 4415 rectangular wing mounted on top of it, its leading edge being at $x = 700$ mm. Fig. 3 shows this model in the test-section. The chord length of the wing, c, was 300 mm and its span, $b = 1600$ mm. The angle between the wing chord and the longitudinal axis of "Model B" was $I_w = 3^\circ$. Using the wind tunnel balance, the three force components (lift, drag and side-force) were measured for various pitch (α), yaw (θ) and roll (φ) angles.

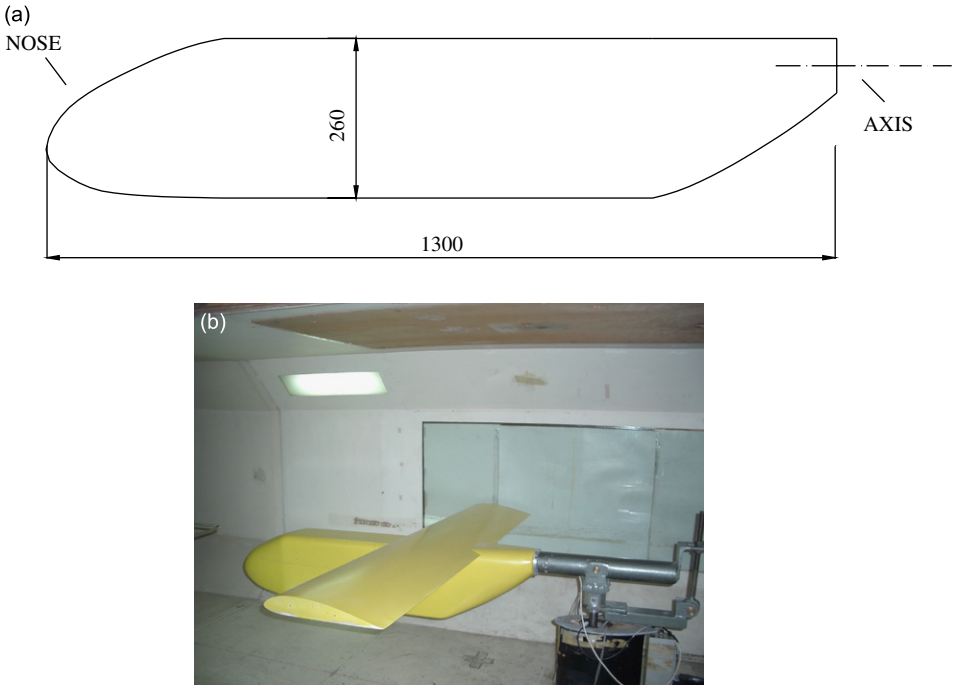

Fig. 3. Model B: (a) longitudinal cross-section; dimensions in mm. (b) Picture of model C (consisting of model B and a NACA wing).

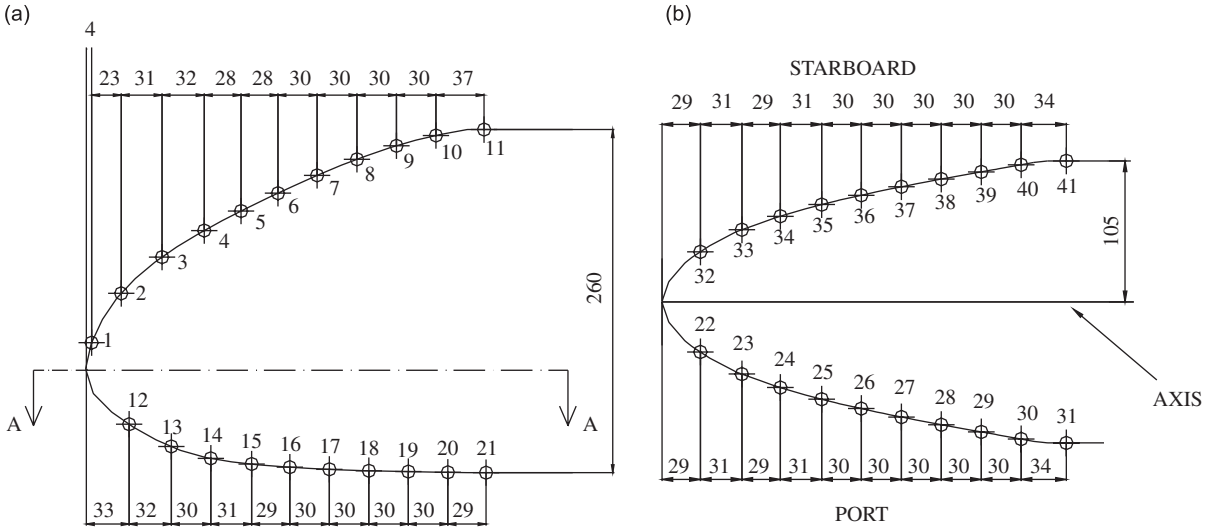

Fig. 4. Model B: nose area pressure orifice locations: (a) vertical symmetry plane and (b) horizontal plane; dimensions in mm.

3. Results and discussion

3.1. Model A

"Model A" was examined at a mean Reynolds number 3.38×10^4 based on the reference length $\ell_{rA} = 33.85\,\text{mm}$, which is the diameter of a circle whose area is equal to the afterbody cross-section. No corrections were made due to

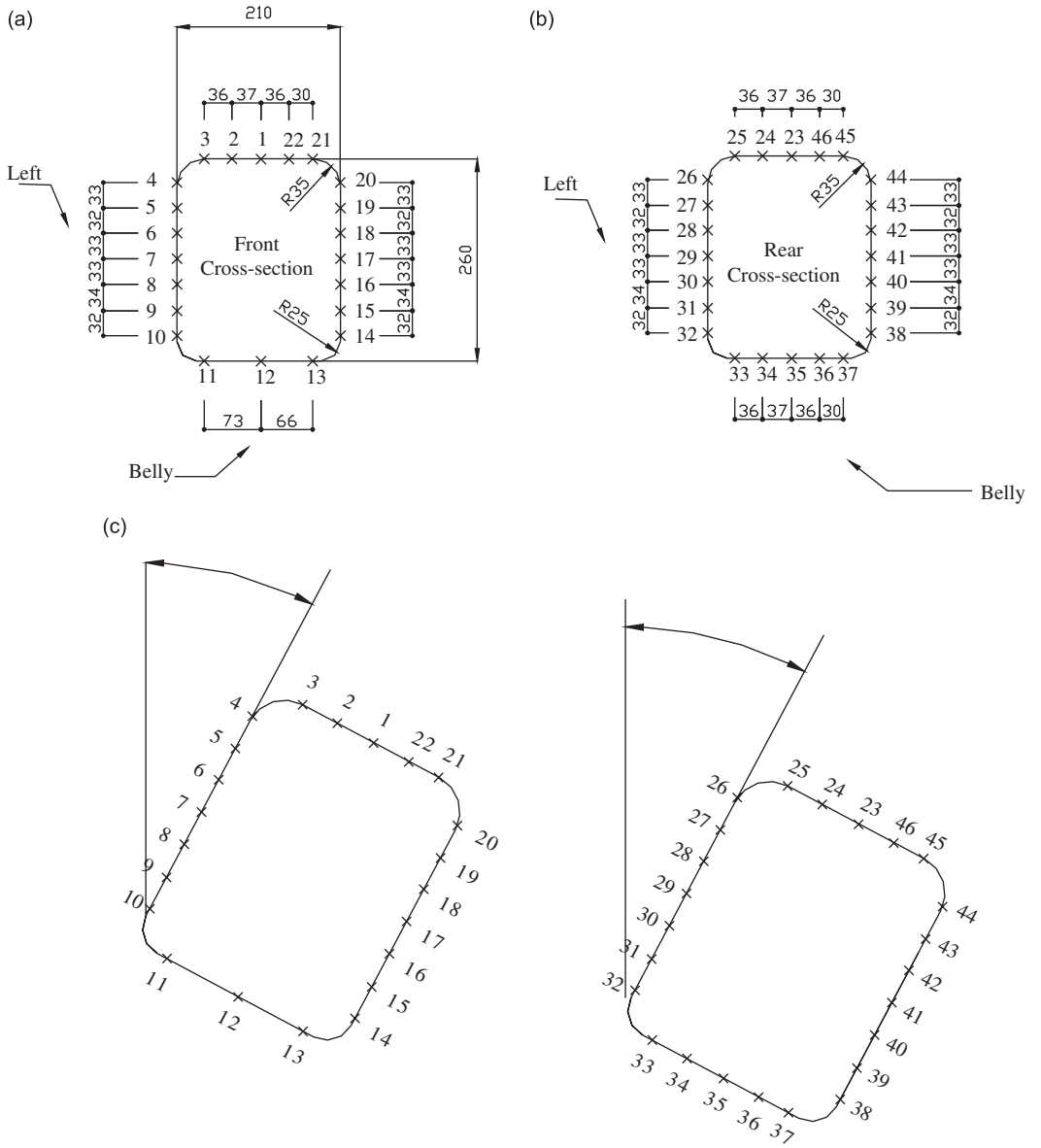

Fig. 5. Model B: pressure orifice locations at (a) the front and (b) rear cross-sections. (c) The two cross-sections at an arbitrary positive roll angle.

blockage, since the maximum ratio of the model frontal area to the tunnel cross-section was smaller than 5% for all the examined body orientations.

Using surface flow visualization, it was found that, independently of the pitch or roll angle, there is always a separation bubble at the junction of the body nose with the afterbody, at its leeside (side A, Fig. 2). The flow separates along the whole length of this side and reattaches along a line which resembles the letter M (Fig. 6). Namely, reattachment occurs earlier on the symmetry plane (pressure port 2, Fig. 2), exhibiting the three-dimensional character of flow separation. The streamwise length of this region shrinks when the body is rolled, being reduced by as much as 50% (Fig. 7), most probably due to the presence of vortices which provide momentum to the otherwise almost stagnant fluid of the separation bubble. A similar phenomenon was also observed in "Model B", despite its curved corners (Fig. 18). For any pitch angle (in the examined range 0–30°) and for zero roll angle, flow separation also takes place in the nose area (see Fig. 8) along the two edges which are adjacent to the leeside edge (sides B and D, see Fig. 2).

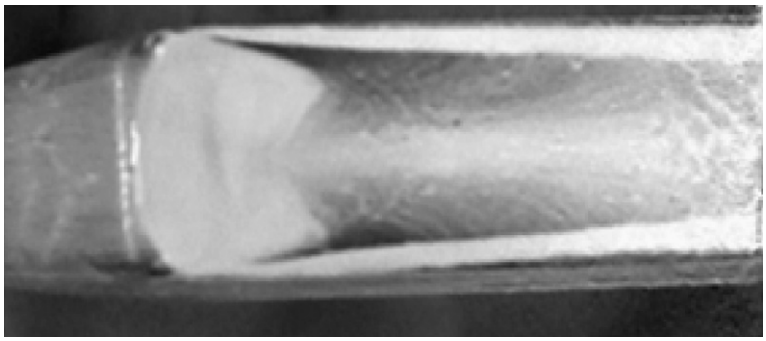

Fig. 6. Model A: separation bubble at the leeside nose–body junction (pitch = 30°, roll = 0°); flow from left to right.

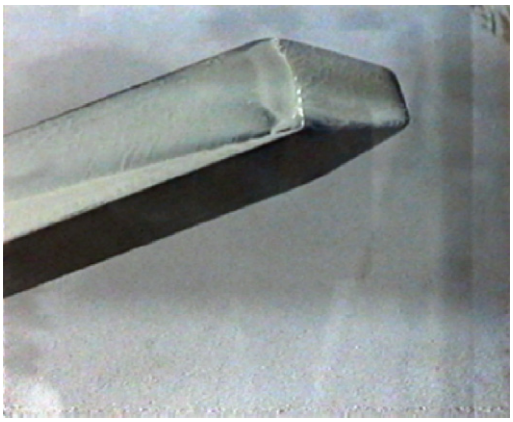

Fig. 7. Model A: separation bubble at the leeside nose–body junction (pitch = 30°, roll = 20°); flow from right to left.

Fig. 8. Model A: flow separation at the nose–body junction next to leeside edge (pitch = 20°, roll = 0°); flow from left to right.

However, rolling the body these separation regions shrink, and especially the one which belongs to the pressure side disappears.

At $\varphi = 0^\circ$, two counter-rotating vortices emanate from the windward side and two other from the leeward side, as a result of cross-flow separation. The traces of the leeside vortices for $\alpha = 30^\circ$ are shown in Fig. 9(a) (side A), whereas those emanating from the windward side in Fig. 9(b) (side B). The leeside vortices are also depicted in Fig. 10 at $x = 120$ mm using smoke visualization, for the same pitch angle. The measured cross-flow velocity field, 10 mm

downstream of the body, is illustrated in Fig. 11 for this particular case ($\varphi = 0^\circ$, $\alpha = 30^\circ$), using the seven-hole Pitot tube. These vortices appear to be weak, in contrast to other roll orientations. Namely, keeping α constant, an increase in roll angle increases the strength of these vortices and at the same time it displaces their centres with respect to the body surface. This is clearly shown in Fig. 12(a)–(c) for roll angles $\varphi = 20^\circ$, 40° and 60° and $\alpha = 30^\circ$. At $\varphi = 20^\circ$, the vortex on the left (port side) is located closer to the body compared to the right one. As a result, a side-force is generated pointing to the left due to low pressures induced by the closer to the body located vortex. Namely, rotating the body in the clockwise direction, a side-force appears pointing to the left. However, at a roll angle of 45°, the two vortices tend to be symmetrically positioned with respect to the body cross-section diagonal, thus minimizing the side-force. On the other hand, due to low pressures induced by the leeside vortices the lift takes high values. A further increase in roll angle, beyond 45°, results in a change of the side-force direction pointing to the port side, since in this case the vortex on the right is closer to the body. Cross-flow velocities took maximum values at the vortex cores being 80% greater than the streamwise velocity component. Reducing the pitch and roll angles, the cross-flow velocities are reduced as well. The change of the vortex locations with φ is clearly depicted in Fig. 13(a)–(c) using smoke visualization at $x = 120$ mm.

A picture of the aerodynamic force variation as a function of the roll angle was obtained through the static pressure distribution p, along the circumference of a cross-section at $x = 150$ mm. Fig. 14(a)–(c) illustrates the distribution of the pressure coefficient, $c_p = (p - p_\infty)/q$ (where q is the free-stream dynamic pressure) at $\alpha = 20^\circ$, and $\phi = 20^\circ$, 40° and 60°, respectively. The horizontal axis of each graph in Fig. 14 refers to the pressure orifice numbers 1–12. At $\varphi = 20^\circ$, pressures 1–3 (side A, see Fig. 2) are higher than those on side D (pressures 10–12). Moreover, the pressures on sides B

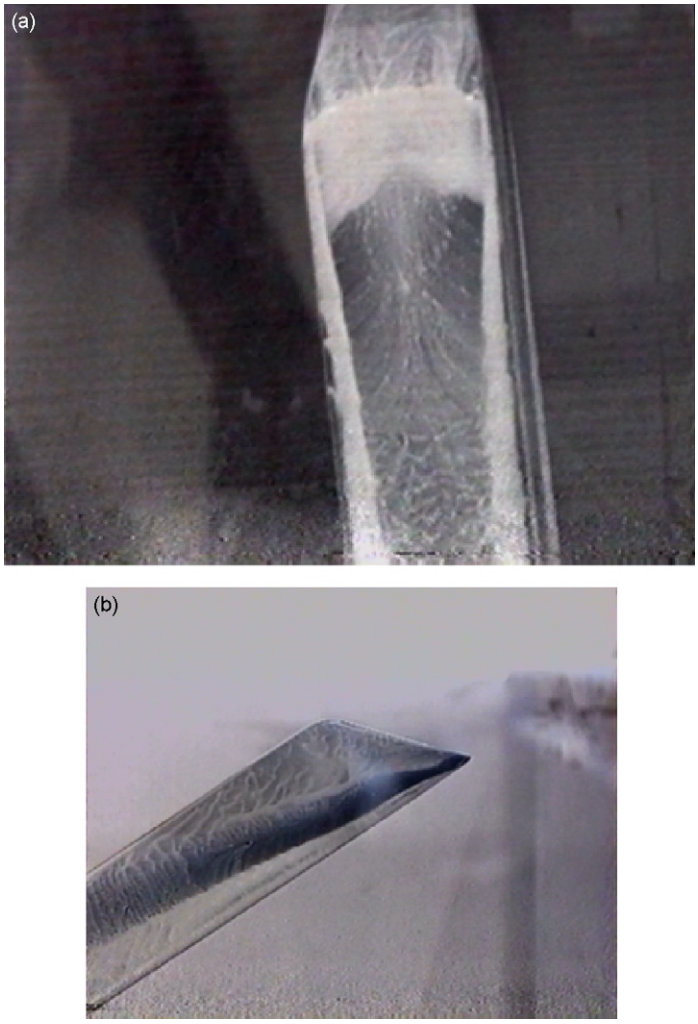

Fig. 9. (a) Model A: vortex traces (pitch = 30°, roll = 0°): (a) leeside wall A (flow from top) and (b) side wall B (flow from right to left).

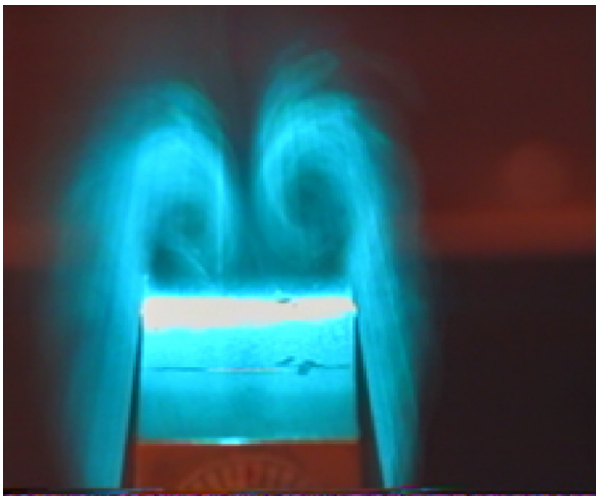

Fig. 10. Model A: vortices on the leeside (pitch = 30°, roll = 0°, $x = 120$ mm).

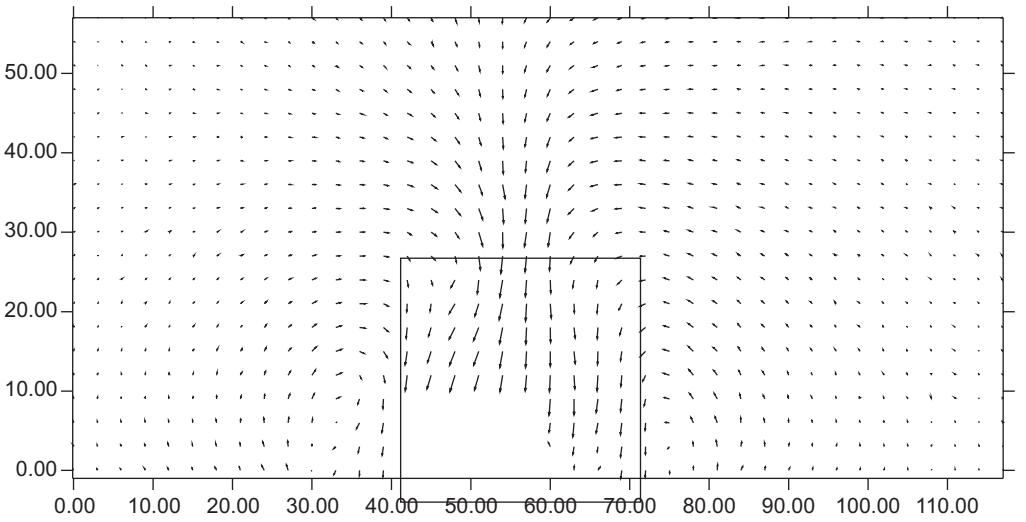

Fig. 11. Model A: cross-flow velocity vectors (pitch = 30°, roll = 0°); dimensions in mm.

and C are even higher since they belong to the windward side of the body for this particular orientation. At a roll angle of 40°, the asymmetric pressure distribution is limited; whereas at roll 60°, the picture reverses in a sense that pressures on side D are higher than those on side A. A common feature of these three cases is the high pressure gradients at the corners, as has also been documented by Wilcox et al. (2004). It is worthy of mentioning that a similar picture of the pressure distribution is obtained in the case of the examined model B, although this model is 10 times larger and the corners are rounded.

3.2. Model B

Details of the flow field about "Model B" for various orientation angles (α, φ, θ) were revealed through pressure distribution, flow visualization and force measurements. Mean Re was 3.24×10^5, based on reference length $\ell_{rB} = 261.74$ mm which is the diameter of a circle whose area is equal to the cross-section of the afterbody.

The pressure variation in the nose area along four lines (see Fig. 4) is shown in Figs. 15–17 for various body orientations. Fig. 15 refers to $\varphi = 0°$, $\theta = 0°$ and $\alpha = 0°$, 5°, 10°, 15° and 20°. As expected, due to the nose-curved

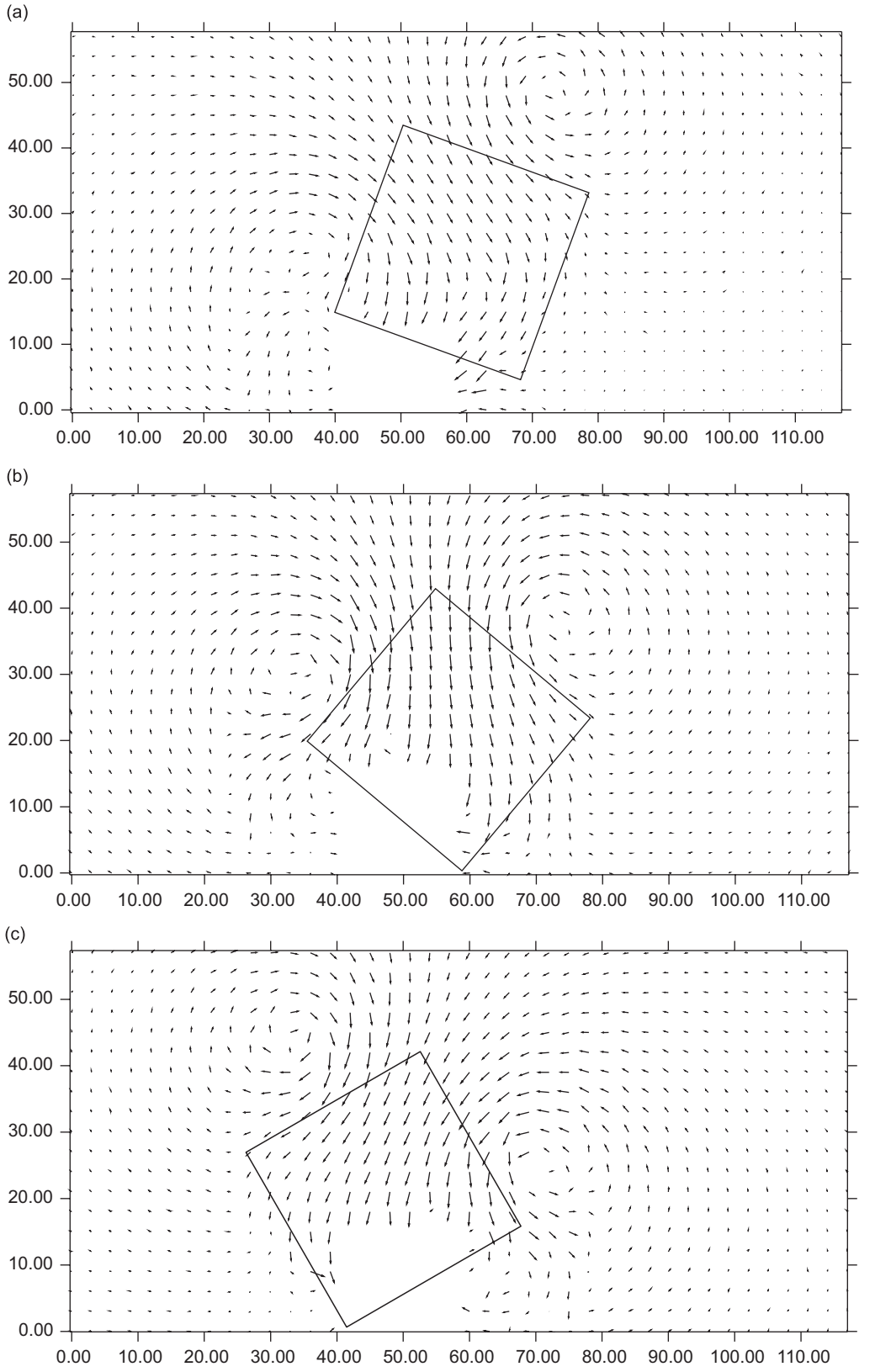

Fig. 12. Model A: cross-flow velocity vectors for pitch = 30°: (a) roll = 20°, (b) roll = 40°, and (c) roll = 60°; dimensions in mm.

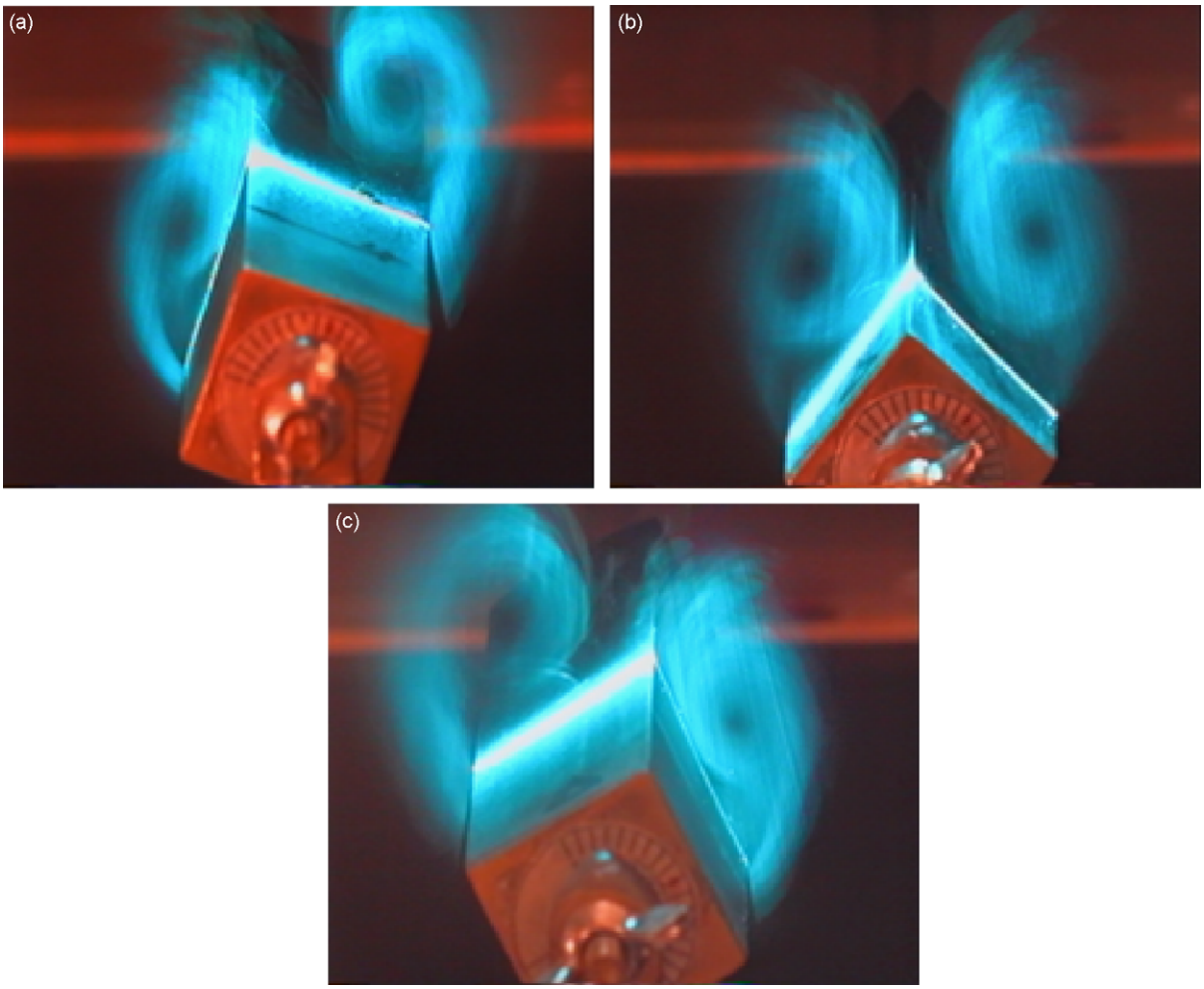

Fig. 13. Model A: leeside vortices at pitch = 30°: (a) roll = 20°, (b) roll = 40°, and (c) roll = 60°.

surface, the pressure on the leeside symmetry plane (pressure orifices 1–11) varies with a high rate at both the nose tip (pressure orifices 1–3) and at the junction with the afterbody (pressure orifices 7–11). In between, the pressure gradient is smaller, and especially at high pitch angles ($\alpha = 15^\circ$ and 20°) it exhibits a local maximum, most probably due to a local separation bubble. At the end of the nose area, the pressure on the same plane increases for all the examined pitch angles. This is attributed to the fact that there is always a separation bubble at the nose–afterbody junction at the leeside, independently of the pitch angle. This flow separation region is illustrated in Fig. 18 through surface flow visualization. It is reminded that such a bubble was always present in "Model A".

The flow in the windward side symmetry plane (pressure orifices 12–21, see Fig. 15) accelerates in the nose tip area and then it decelerates due to a separation bubble for $\alpha = 0$–15°, showing a pressure local maximum. This separation seems to be absent for $\alpha = 20^\circ$, since the pressure drops, in this case, monotonically in the whole length of the nose. With regard to the nose left (port) side (pressure ports 22–31) and right (starboard) side (pressure ports 32–41), the pressures in the nose area are almost symmetric, with a maximum deviation of 0.04 for c_p between symmetric locations (Fig. 15). Also, the pressure gradient on these sides is negative, taking higher values close to the nose as well as at the junction with the afterbody.

Asymmetric loading does appear when rolling the body. Changing the roll angle from 0° to 20° and keeping $\alpha = 20^\circ$, the pressures on the left side of the nose drop (pressure ports 22–31), whereas those on the right side increase (Fig. 16). This can be attributed to the fact that rolling the body clockwise, the right side tends to become the windward side of the body with a consequence a pressure increase. However, the pressure field on the symmetry plane is less affected for the examined roll angle variation (Fig. 16).

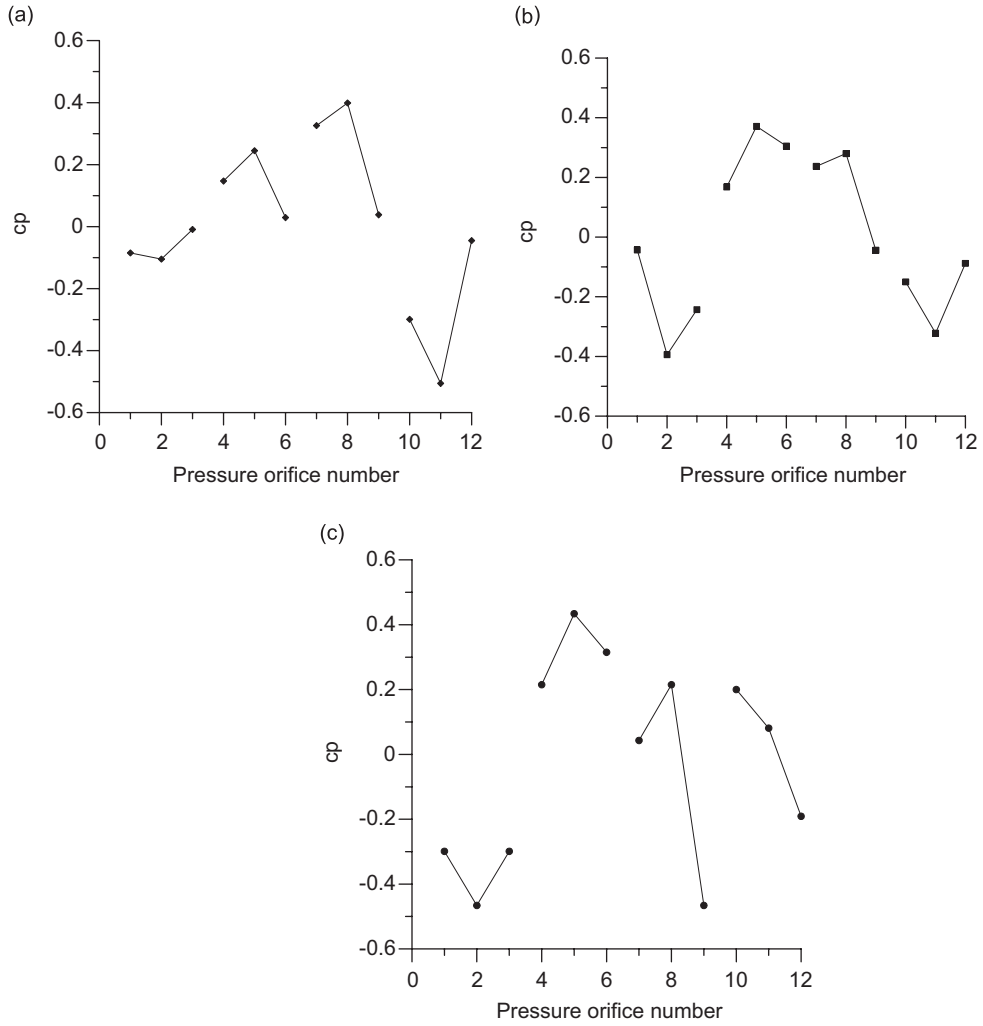

Fig. 14. Model A: pressure distribution for pitch = 20°: (a) roll = 20°, (b) roll = 40°, and (c) roll = 60°.

When the body yaw angle becomes 10° (movement of the nose tip to the right), the pressures on the nose symmetry plane vary more or less like in the zero yaw angle case (Fig. 17). However, major differences do appear on the left and right side, with the left one presenting much higher values compared to the right one. The small range of pressure values in the right side manifests the existence of a separation region, which appears for the whole range of the examined pitch angles.

The flow evolution in the afterbody is studied through the pressure distributions at two cross-sections, namely at $x = 290$ mm (at the nose–afterbody junction) and $x = 590$ mm (Fig. 5). For zero roll and yaw angles, Fig. 19 illustrates the major flow characteristics in this part of the body, namely (a) significant pressure gradients appear at the four corners of the cross-section, exhibiting pressure local minima there, (b) pressure shows a local maximum on each side of the cross-section, (c) within the experimental uncertainty, the pressure distribution is practically symmetric, (d) increasing α, the pressure on the windward side increases whereas on the other three sides it drops, especially on the leeside, (e) there is a pressure recovery in the longitudinal direction (pressures at $x = 590$ mm are higher than at $x = 290$ mm). When the body is rolled towards the starboard side, asymmetric loading becomes evident shown in Fig. 20, with the starboard side presenting higher pressures, compared to the port side. On the windward side the maximum of the pressure appears at the lowest point of the cross-section whereas at the leeside a pressure minimum is located at the lower edge of this side. It is worthy to mention that a similar behaviour of the pressure distribution was recorded by Wilcox et al. (2004) for a square cross-section missile at supersonic speeds ($M = 2.5$ and 4.5).

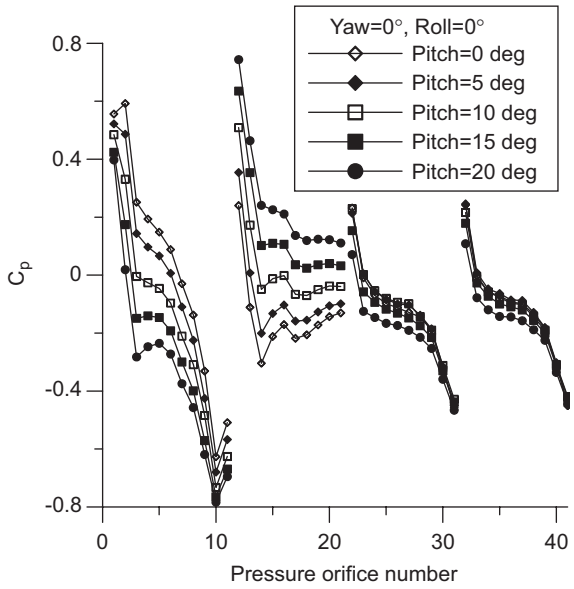

Fig. 15. Model B: pressure distribution in nose area (roll = 0°, yaw = 0°, pitch = 0–20°).

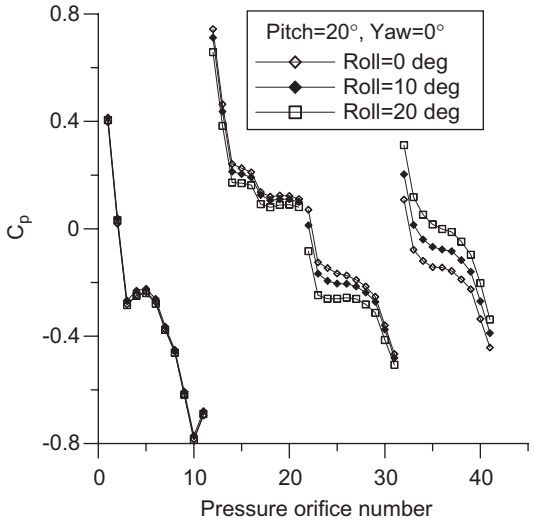

Fig. 16. Model B: pressure distribution in nose area (pitch = 20°, yaw = 0°, roll = 0–20°).

Using surface flow visualization on the left side of this model (Fig. 21) for $\varphi = 20^\circ$ and $\alpha = 20^\circ$, the picture is similar with that of the much smaller model A (see Fig. 9(b)). Namely, the accumulation of the white TiO_2 powder along a line in the lower part of this side reflects the low wall shear stress values of this region associated with the existence of a cross-flow vortex close to the body.

Besides pressure measurements, the aerodynamic forces exerted on the body, namely lift, drag and side-force were measured as well and the corresponding aerodynamic coefficients. The calculation of these coefficients was based on the free-steam velocity and the reference area $S_B = 0.0538\,m^2$, which is the cross-sectional area of the afterbody. The free-stream velocity was corrected (see Appendix A) due to the model solid and wake blockage, according to a procedure described by Rae and Pope (1984). The three force coefficients are shown in Fig. 22 for $\alpha = 20^\circ$ and $\varphi = 0$–45° with a 5° step. It is noticeable that the side-force maximizes for roll angles between 20° and 25°, the drag increases with the roll

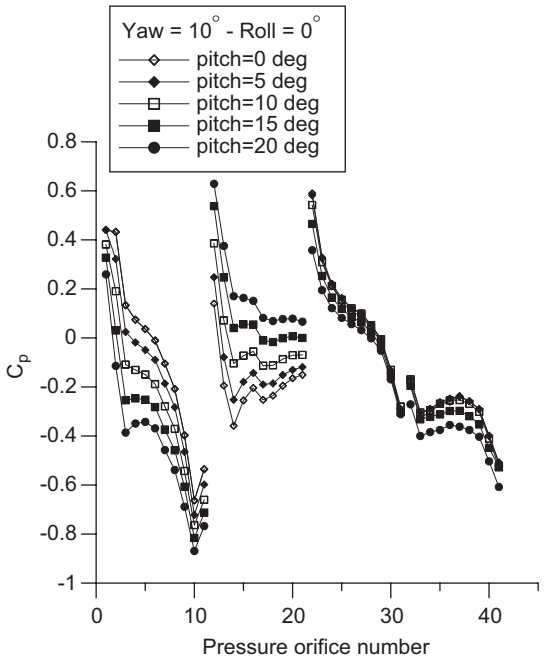

Fig. 17. Model B: pressure distribution in nose area (yaw = 10°, roll = 0°, pitch = 0–20°).

angle due to the increase of the exposed area, and the lift increases due to the low pressures induced by the leeside vortices. Based on L and D, the normal force coefficient was calculated, being increased 5.7 times in the interval $\varphi = 0$–45°. Comparing the normal force increase with that one applied on square section bodies in the transonic regime ($M = 0.9$) (Jackson and Sawyer, 1992), it is about three times greater. This difference might be attributed to compressibility effects or to the much different Re numbers.

3.3. Model C

In this case, force measurements and flow visualization were performed at a mean $\mathrm{Re} = 3.74 \times 10^5$ based on the wing chord length $c = 300\,\mathrm{mm}$. The wing planform area $S_w = 0.3\,\mathrm{m} \times 1.6\,\mathrm{m} = 0.48\,\mathrm{m}^2$ was used in the calculation of the force coefficients.

This model is a combination of model B and an NACA 4415 wing attached on its leeside at an angle of 3° (see Fig. 3). Having studied the flow characteristics about Model B, this paragraph examines its influence on the aerodynamics of the wing-body configuration, which essentially constitutes the major part of an existing UAV (elevators, rudder and engine are not included in model C).

Due to the solid-wake blockage and the wing circulation effect, the free-stream velocity was corrected for each model orientation as well as the lift-pitch angle curve (see Appendix B). The corrected C_L versus α curve is shown in Fig. 23, the linear part of which is given by the relationship

$$C_L = 0.0807\alpha + 0.49, \tag{1}$$

where α is in degrees. It is concluded, from the above formula, that the zero lift angle is -6.07° and the lift slope $4.62\,\mathrm{rad}^{-1}$. For an infinite aspect ratio NACA 4415 airfoil, the zero lift angle is -4° (Abbott and Von Doenhoff, 1958). Since this angle is not affected by the wing aspect ratio or the Reynolds number (Rae and Pope, 1984, p. 461), it is the wing-body combination which makes this difference. Also, it was found that the wing-body lift curve slope is higher than that of the wing alone. Namely, for $\mathrm{Re} = 2 \times 10^6$ an infinite aspect ratio NACA 4415 wing has a lift slope $C_{L\alpha} = 6.019\,\mathrm{rad}^{-1}$ (Abbott and Von Doenhoff, 1958) and for the aspect ratio $A = 1.6/0.3 = 5.33$ of the examined rectangular wing this is (Torenbeek, 1982):

$$C_{Lw\alpha} = \frac{C_{L\alpha}}{1 + (1/A) + (C_{L\alpha}/\pi A)} = 3.89\,\mathrm{rad}^{-1}. \tag{2}$$

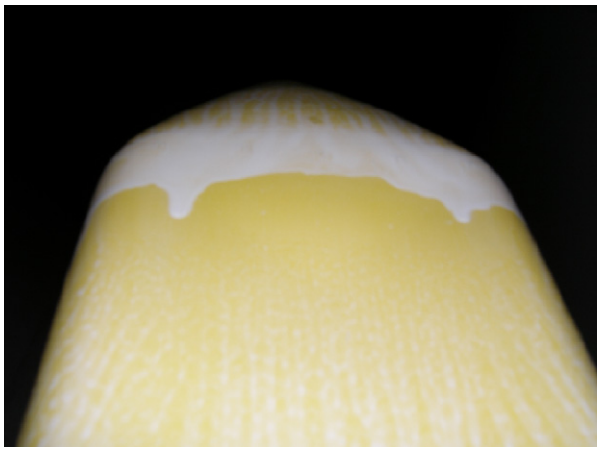

Fig. 18. Model B: separation bubble at the nose–afterbody junction leeside (pitch = 20°, roll = 0°, yaw = 0°).

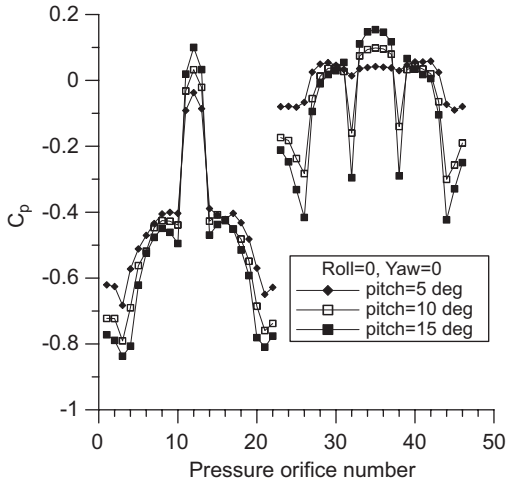

Fig. 19. Model B: pressure distribution at two cross sections (roll = 0^0, yaw = 0^0, pitch = 5°, 10°, 15°).

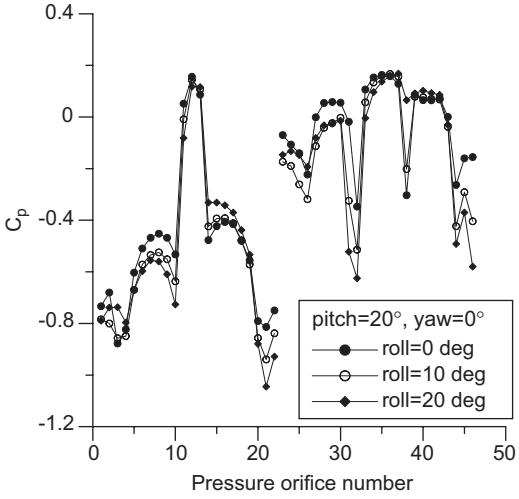

Fig. 20. Model B: pressure distributions at two cross sections (pitch = 20°, yaw = 0°, roll = 0–20°).

Fig. 21. Model B: flow visualization on port side for pitch = 20° and roll = 20°; flow from left to right.

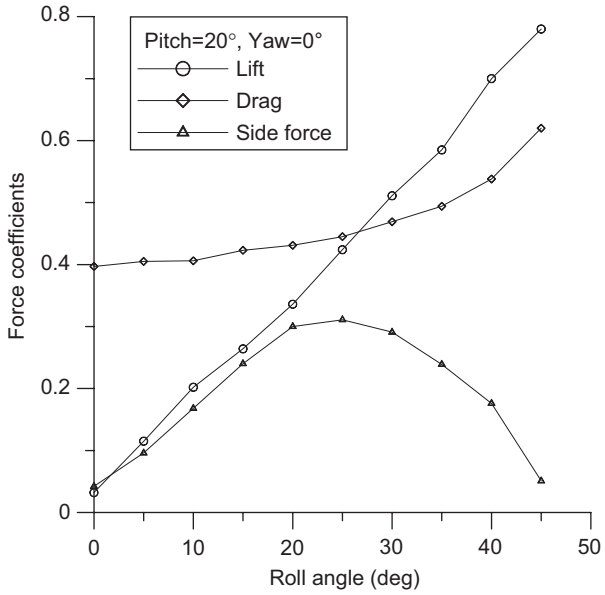

Fig. 22. Model B: lift, drag and side-force coefficients (pitch = 20°, yaw = 0°, roll = 0–45°).

It is known that the lift slope is reduced slightly when Re is reduced. Therefore, the lift slope of the wing alone is expected to be lower than $3.89\,\mathrm{rad}^{-1}$ given the fact that the examined Re was 3.74×10^5, namely much lower than 2×10^6. Therefore, the increase in the lift slope due to the wing-body combination from 3.89 to $4.62\,\mathrm{rad}^{-1}$ will be even higher.

An estimate of the wing-body lift curve was also obtained from Torenbeek (1982, p. 479), according to which the lift coefficient C_{Lwf} is given by

$$C_{Lwf} = k_{\mathrm{I}} C_{Lw\alpha}\left[\alpha + \frac{k_{\mathrm{II}}}{k_{\mathrm{I}}}(I_w - \alpha_0)\right] + \Delta z C_L, \tag{3a}$$

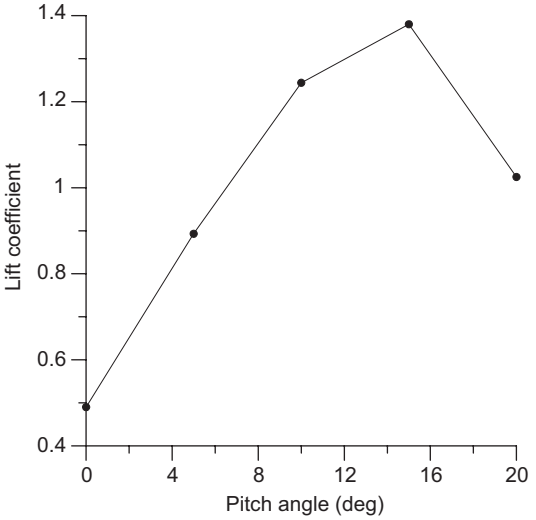

Fig. 23. Model C: corrected lift curve.

where

$$k_{\mathrm{I}} = \left(1 + 2.15\frac{b_f}{b}\right)\frac{S_{\mathrm{net}}}{S} + \left(\frac{\pi}{2C_{Lw\alpha}}\right)\frac{b_f^2}{S}, \quad k_{\mathrm{II}} = \left(1 + \frac{0.7b_f}{b}\right)\frac{S_{\mathrm{net}}}{S}, \tag{3b}$$

with α the pitch angle of the fuselage, $S = S_w = 0.3\,\mathrm{m} \times 1.6\,\mathrm{m} = 0.48\,\mathrm{m}^2$ the wing planform area, $b = 1.6\,\mathrm{m}$ the wing span, $b_f = 0.21\,\mathrm{m}$ the length of the wing which is attached to the fuselage, $S_{\mathrm{net}} = S - 0.21\,\mathrm{m} \times 0.3\,\mathrm{m} = 0.417\,\mathrm{m}^2$ is the area of the wing having subtracted its part which is attached to the fuselage, $I_w = 3\pi/180$ is the angle (in rad) of the wing chord with respect to the fuselage longitudinal axis, $\alpha_0 = -4\pi/180$ is the zero lift angle of the NACA 4415 airfoil and

$$\Delta z C_L = -0.1c\frac{b_f}{S} = -0.1 \times 0.3 \times 0.21/0.48 = -0.0131, \tag{3c}$$

with $c = 0.3\,\mathrm{m}$ the wing chord.

The last term applies for high-wing configurations like the examined one. Therefore, the linear part of the lift curve of the wing-body configuration is estimated to be

$$C_{Lwf} = 4.477\alpha + 0.437, \tag{4}$$

where α is in rad. According to Eq. (4), the slope of the wing-body configuration is $4.477\,\mathrm{rad}^{-1}$ and the angle for zero lift -5.59°, which are compared well with the experimentally found $4.62\,\mathrm{rad}^{-1}$ and -6.07°, respectively. Increasing Re, the lift slope does not change substantially, so that this information obtained from the experiment can be also used, with regard to the linear part of the lift curve, for a full-scale configuration.

The drag coefficient due to the induced drag was corrected, according to the following formula (Rae and Pope, 1984, p. 379):

$$C_D = C'_D + \frac{\delta S}{C}C'^2_L. \tag{5}$$

For more details see also Appendix B. After making all the above corrections, the drag polar is presented in Fig. 24. Based on this figure, the linear part of C_D versus C_L^2 is given by the formula

$$C_D = 0.0083 + 0.067C_L^2. \tag{6}$$

For higher Reynolds numbers, the above formula will not change with regard to the coefficient 0.067 of the non linear term, since $(1/A)(\mathrm{d}C_D/\mathrm{d}C_L^2)$ is Reynolds independent (Rae and Pope, 1984, p. 457). On the other hand, the constant 0.0083 is expected to be reduced since the so-called parasite drag drops with increasing Re.

Since the aerodynamic forces exerted on the fuselage (Model B) increase with the pitch and roll angles, its influence on "Model C" was examined for the highest pitch angle (20°) and roll angles 0–45°. As it is shown in Fig. 25, the lift and

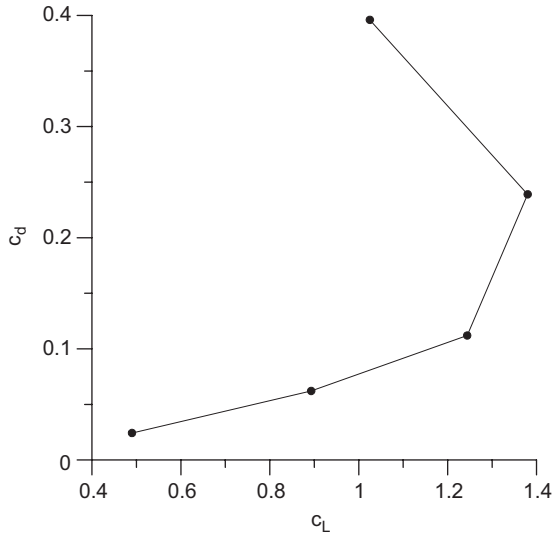

Fig. 24. Model C: corrected drag polar plot.

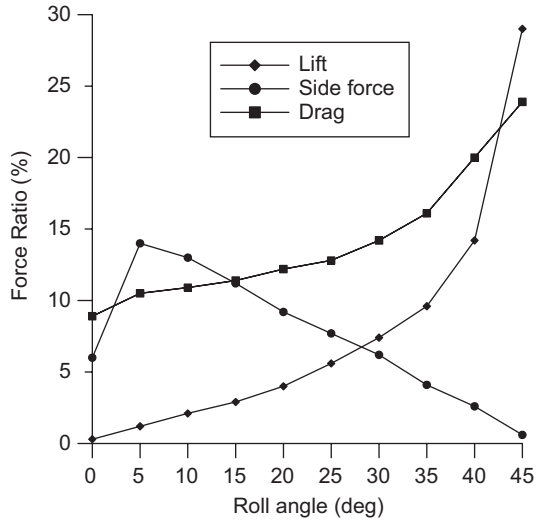

Fig. 25. Models B–C force ratio (pitch = 20°).

drag applied on the fuselage (namely on model B) is at most 30% of that applied on model C, whereas the side-force is much lower (at most 15%). It is noticeable that the "Model C" side-force increases with the roll angle (see Fig. 26), without showing any maximum value, in contrast to models A and B. However, the rate at which the side-force increases is reduced in the roll angle interval 20–30°. A plausible explanation of this behaviour might be the fact that the side-force applied on the fuselage maximizes at a roll angle of about 25° and it points in the opposite direction from that applied on the wing.

4. Conclusions

The flow field around three models was examined experimentally, namely a square section body with sharp edges, a rectangular one (1:1.23) with rounded edges, and a high wing-body configuration. The tools used in this study were flow visualization, velocity, pressure, and force measurements. Using a seven-hole Pitot tube, a good picture of the vortex

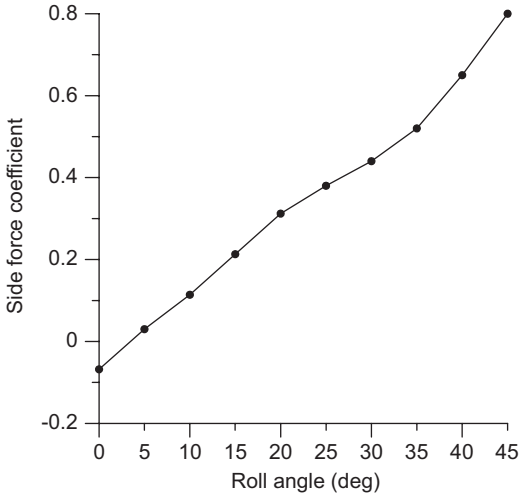

Fig. 26. Model C: side-force coefficient versus roll angle (pitch = 20°, roll = 0–45°).

dominated wake was obtained, although a noninvasive technique like PIV or LDA would be a more suitable tool especially close to the walls of the model.

With regard to models A and B (the dimensions of which differed one order of magnitude), the basic flow features were similar, as follows.

(i) A flow separation bubble always existed at the nose–afterbody leeside junction for all body orientations.
(ii) No asymmetries were practically detected for a zero roll angle and pitch angles up to 20°, based on pressure and force measurements, at nonzero roll and yaw angles, pressure asymmetries do appear both at the nose and the afterbody. The maximum side-force occurs at a roll angle of about 25°.
(iii) High pressure gradients exist at the corners of the body cross-section which end up with low pressures at these locations. Also, local pressure maxima appear on each side of the body cross-section.
(iv) Two counter-rotating vortices dominate on the leeside of the body, getting stronger with increasing pitch and roll angles.

The influence of the fuselage (model B) on the aerodynamics of a fuselage–wing combination (model C) is summarized as follows.

(a) For a zero roll angle, the lift is higher compared with the wing-alone case, namely the lift slope of model C is higher by 20% and the zero lift angle is more negative by 2°.
(b) Increasing the roll angle while keeping the pitch angle constant, the side-force on model C increases monotonically, in contrast to models A and B for which a maximum appears. However, the rate at which the side-force increases is reduced in the roll angle interval of 20–30°.
(c) No asymmetries were practically detected for a zero roll angle and pitch angles up to 20°.

Appendix A: Model B: solid-wake blockage correction

Due to the solid wind tunnel walls, the dynamic pressure of the free stream that model B is exposed to is higher than the measured one. This increase is estimated following the procedure described by Rae and Pope (1984). Namely, solid blockage correction was applied first, attributed to the model volume which speeds up the flow due to the reduced test-section area. Then, wake blockage correction followed, due to the reduced pressure downstream of the body (compared to the unlimited case), which practically speeds up the flow as well (Maskel, 1963). An estimate of the speed increase ΔU of the measured free-stream velocity U^* due to the solid blockage is given by (Rae and Pope, 1984, pp. 364–366):

$$\left(\frac{\Delta U}{U^*}\right)_s = \frac{k_3 \tau_1 V}{C^{3/2}}, \tag{A.1}$$

where $k_3 = 0.94$, a parameter dependent on the ratio of the body diameter to the body length, $\tau_1 = 0.85$, a parameter which is a function of the test-section shape, $C = 2.37\,\mathrm{m}^2$, the tunnel cross-sectional area and V, the volume of the model. In this case $V - V_B$, the volume of model B. Therefore, $(\Delta U/U^*)_s = 1.19\%$. The wake blockage is a function of the body orientation, depending on both the measured drag coefficient C_D^* and the body frontal area. According to Maskel (1963), the increase of the free stream due to the wake blockage is

$$\left(\frac{\Delta U}{U^*}\right)_w = \left(1 + \frac{\varepsilon S}{C} C_D^*\right)^{1/2} - 1, \tag{A.2}$$

where $\varepsilon = 2.5$ is a typical value for three-dimensional bodies and S, the body frontal area. Applying formulas (1) and (2), for the extreme cases that the body was at a pitch angle of 20° and a roll angle of 0°, the sum of the solid and wake blockage was 2.8%, whereas for roll 45°, this was 7.2%. The corresponding increase of the free-stream dynamic pressure which is used in the definition of the force coefficients was apparently twice as much, namely 5.6% and 14.4%.

Appendix B: Model C: solid-wake and vortex blockage corrections

Regarding solid blockage in the case of model C, this is the sum of the body solid blockage, which was estimated to be equal to 1.19%, and the wing solid blockage (Rae and Pope, 1984, p. 366). According to Rae and Pope (1984, pp. 364–366), the latter is estimated through Eq. (A.1), where the parameter k_3 for a four digit NACA airfoil with a maximum thickness to chord ratio 15%, like the one examined, is 1.035. Also, $\tau_1 = 0.9$, based on the ratio of the model wing span to tunnel breadth and the given tunnel cross-section shape. Therefore, applying Eq. (A.1) and considering that $V = V_w$ the wing volume, the free-stream velocity increase is estimated to be $(\Delta U/U^*)_s = 0.38\%$ and consequently, the total solid blockage for "Model C" is 1.578%.

According to a method proposed by Maskel (1963), the wake blockage is

$$\left(\frac{\Delta U}{U^*}\right)_{wake} = 0.25\frac{S}{C} C_{D0}^* + \left(\frac{1.25S}{C}\right)(C_D^* - C_{Di}^* - C_{D0}^*), \tag{A.3}$$

where C_{Di}^* is the vortex drag coefficient, being proportional to the squared lift coefficient C_L^{*2}, and C_{D0}^* the drag coefficient for zero lift. The asterisks in the symbols refer to uncorrected (measured) values. The second term on the right hand side of Eq. (A.3) refers to the wing stalled case. In this equation, the wing planform area S_w is taken as the reference area, and $C = 2.37\,\mathrm{m}^2$, the wind-tunnel cross-section. The uncorrected drag polar, Fig. 27, demonstrates that the linear relationship $C_D^* - C_L^{*2}$ holds for pitch angles up to 10° from which it is found that $C_{D0}^* = 0.0065$. Above this angle, the drag increases with a high rate, in contrast to the lift, which increases a little till 15° and then it drops dramatically at 20°, apparently due to deep stall. For pitch angles of 0°, 5° and 10°, only the first term on the right hand side of Eq. (A.3) is nonzero, considering that the flow is attached for these angles. Therefore, the total blockage (solid and wake) when the flow over the wing is attached is 1.578% (solid) + 0.32% (wake) = 1.898%. For higher angles this becomes 5.458% for 15°, and 12.99% for 20°. Based on these figures, the corrected values C_L' and C_D' were obtained, which due to the wing circulation were further corrected. It has to be recalled that the image vortices of the wing bound

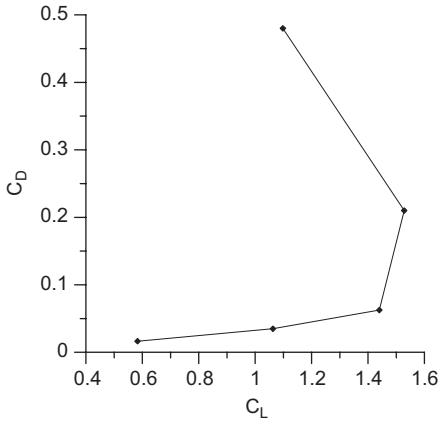

Fig. 27. Model C: uncorrected drag polar plot.

vortex and its tip vortices, which are introduced so that the no penetration condition is satisfied on the tunnel walls, increase the lift and reduce the drag. The lift coefficient was corrected using the C'_L versus α' curve in which the geometric pitch angle α^* was increased by a certain amount, according to the formula (Rae and Pope, 1984, p. 379):

$$\alpha = \alpha^* + 57.3\frac{S\delta}{C}C_L, \tag{A.4}$$

where α^* is in deg and $\delta = 0.135$ based on the test-section shape and the wing span. The increase of the pitch angle was between 0.87° and 2.17° for the examined pitch angle range (0–20°).

References

Abbott, I.H., Von Doenhoff, A.E., 1958. Theory of Wing Sections. Dover Publications, Inc., New York.

Daniel, D.C., Yechout, T.R., Zollars, G.J., 1982. Experimental aerodynamic characteristics of missiles with square cross sections. Journal of Spacecraft and Rockets 19, 167–172.

Daniel, D.C., Zollars, G.J., Yechout, T.R., 1984. Reynolds number effects on the aerodynamics of a body with square cross-section. Journal of Spacecraft and Rockets 21, 413–414.

Ericson, L.E., Reding, J.P., 1986. Asymmetric vortex shedding from bodies of revolution. In: Hemsch, M.J., Nielsen, N.J. (Eds.), Tactical Missile Aerodynamics Progress in Astronautics and Aeronautics, vol. 104. AIAA, New York, pp. 243–296.

Jackson Jr., C.M., Sawyer, W.C., 1992. Bodies with noncircular cross sections and bank-to-turn missiles. In: Hemsch, M.J. (Ed.), Tactical Missile Aerodynamics: General Topics. AIAA, pp. 365–389.

Johansen, E.S., Rediniotis, O.K., Jones, G., 2001. The compressible calibration of miniature multi-hole probes. ASME Journal of Fluids Engineering 123, 128–138.

Lamont, P.J., 1982. Pressures around an inclined to give cylinder with laminar, transitional and turbulent separation. AIAA Journal 20, 1492–1499.

Lijewski, L.E., Zollars, G.J., Yechout, T.R., Haupt, B.F., 1982. Experimental flow field measurements of missiles with square cross sections. AIAA Paper 1982-0055.

Maskel, E.C., 1963. A theory of the blockage effects on bluff bodies and stalled wings in a closed wind tunnel. R&M No. 3400.

Rae, W.H., Pope, A., 1984. Low Speed Wind-Tunnel Testing, second ed. Wiley, New York.

Schneider, W., 1982. Experimental investigation of bodies with non-circular cross section in compressible flow. AGARD CPP 336, Missile Aerodynamics, 19-1–19-11.

Torenbeek, E., 1982. Synthesis of Subsonic Airplane Design. Kluwer Academic Publishers, Dordrecht.

Wilcox, F.J., Birch, T.J., Allen, J.M., 2004. Force, surface pressure, and flow field measurements on a slender missile configuration with square cross-section at supersonic speeds. AIAA Paper 2004–5451.